Rare-gas-cluster explosions under irradiation by intense short XUV pulses

K. Hoffmann, B. Murphy, N. Kandadai, B. Erk, A. Helal, J. Keto, and T. Ditmire*

Department of Physics, Texas Center for High Intensity Laser Science, The University of Texas at Austin, Austin, Texas 78712, USA

(Received 9 August 2010; published 25 April 2011; publisher error corrected 3 May 2011)

High-intensity, extreme-ultraviolet (XUV) femtosecond interactions with large rare-gas clusters of xenon and argon have been studied at a wavelength of 38 nm. Pulses of XUV radiation with nJ energy are produced by high-order harmonic conversion from a 35-fs, near-infrared, terawatt laser. Mass resolved ion spectra show charge states up to Xe^{8+} and Ar^{4+}. Kinetic-energy measurements of ions and electrons indicate that a nanoplasma is formed and a hydrodynamic cluster explosion ensues after heating by the short wavelength pulse. It appears that the observed charge states and electron temperatures are consistent with sequential, single-photon ionization and collisional ionization of ions that have had their ionization potential depressed by plasma continuum lowering in the cluster nanoplasma.

DOI: 10.1103/PhysRevA.83.043203 PACS number(s): 36.40.Gk, 36.40.Qv, 52.50.Jm

I. INTRODUCTION

The nature of the interactions between high-intensity, ultrafast, near-infrared laser pulses and atomic clusters of a few hundred to a few hundred thousand atoms has been well studied over the past few years by a number of groups worldwide [1–3]. Such studies have found some rather unexpected results, including the striking finding that these interactions appear to be more energetic than interactions with either single atoms or solid-density plasmas. Atoms in clusters can absorb large amounts of energy from the laser field, producing x rays, hot electrons, and energetic ions in a process dominated by the large ponderomotive force [1]. At high intensity, the electric field of the laser strips electrons from the cluster by tunnel and barrier suppression ionization. Depending on cluster size and Z constitution clusters explode by Coulomb or hydrodynamic forces. If the ponderomotive potential of the laser exceeds the surface binding potential of the ionized cluster, the laser field removes most of the electrons and the charged cluster explodes by Coulomb forces. This is the case for small cluster sizes and low Z cluster composition [4]. For larger clusters electrons can be confined to the vicinity of the cluster by space-charge forces and further ionize the cluster to high-charge states by collisional ionization, resulting in a "nanoplasma," which explodes by hydrodynamic forces [1].

The availability of free-electron lasers (FEL) and higher-harmonic-generation (HHG) sources have made possible studies of high-intensity short-wavelength pulse interactions with clusters. The extreme ultraviolet (XUV) wavelength range from 10 to 100 nm has been explored by a number of groups [5–15] in the past years. Major differences between XUV and near-infrared (NIR) pulses include high-photon energy and a small ponderomotive potential of the incident field. Mechanisms responsible for the strong cluster reaction to the near-infrared laser field are "turned off" at short wavelengths. Single photoionization becomes the dominating ionization process and can sequentially strip the cluster atoms to high-charge states. However, because of the weak ponderomotive potential, electrons are not easily removed from the cluster's space-charge forces and will be confined in the cluster. It is not clear that a nanoplasma will form as the XUV pulse ejects photoionized electrons sequentially, and it is an open question whether XUV irradiated clusters will explode by Coulomb explosion or by hydrodynamic forces.

One major motivation to study the physics of intense short-wavelength interactions with clusters relates to diffraction imaging of isolated biomolecules by x-ray FELs [5]. A better understanding of the coupling of energy from the light pulse to the atoms and electrons in large clusters will provide needed information about the motion of biomolecule atoms during the x-ray exposure.

Experiments on intense, short wavelength irradiated clusters have been performed at the DESY VUV-FEL in 2002 with Xe clusters of sizes ranging up to ~30 000 atoms per cluster [6–8]. This experiment yielded the surprising result that energetic electrons and high ion-charge states (Xe^{8+}) are produced when clusters are irradiated with 95-nm light at intensities of $\sim 10^{13}$ W/cm^2 [6] and that the mechanism for ejecting the high Xe charge states from the clusters was by a Coulomb explosion. Further measurements taken at 95 nm showed that electrons emitted from moderately sized (~1000 atom) Ar and Xe clusters had a quasi-Maxwellian distribution with a 9-eV electron temperature [8]. Later experiments in the mid XUV at 33 nm in small (<200 atom) Ar clusters have been reported with a different conclusion, the electron removal from the cluster appeared purely sequential, and the authors saw little evidence for the production of a nanoplasma (except at the highest intensities above 5×10^{13} W/cm^2) nor a thermal electron distribution [9]. More recent experiments in the soft x-ray range at 13.6 nm with Xe clusters (<10 000) concluded again the generation of a nanoplasma, where highly charged surface ions explode by Coulomb forces and the inner core expands by hydrodynamic forces [10].

Many theoretical studies focused particularly on the unusually high absorption and the high-charge-state production that have been observed in the early DESY experiments. Several distinct models have attempted to explain these results. Thermalized nanoplasma heating by inverse bremsstrahlung (IBS) absorption has been proposed by Santra and Greene (with appropriate corrections to the collision rates) [11]. Siedschlag and Rost have hypothesized that single-photon absorption

*tditmire@physics.utexas.edu

 ©2011 American Physical Society

in the cluster produces the high-charge states assuming that this is facilitated by the distortion of the ionic binding potentials due to neighboring ions in the cluster resulting in larger IBS absorption [12]. Simulations by Bauer [13] revealed that IBS in this picture contributes only to outer ionization. Finally, simulations preformed by Jungreuthmayer *et al.* have indicated that the high-charge states are the results of many-body recombination heating, which is the process of collisional ionization by electron cloud heating [14]. All of these models utilize the formation of a nanoplasma in the cluster, which is not completely supported by the DESY data, which in turn suggests that Coulomb explosion [6,7] may not be the dominating mechanism. In a recent paper, Ziaja *et al.* combine both pictures using a nonequilibrium Boltzmann model [15]. They find that the cluster upon irradiation at 100 nm exhibits an outer shell composed of ions, surrounding a quasineutral plasma formed from the electrons that do not escape the space-charge forces of the cluster. This is a geometry predicted by Breizman *et al.* in NIR irradiated clusters [16]. Ziaja *et al.* find in their simulations that a Coulomb explosion of the outer cluster shell is responsible for observed high-charge states in the DESY experiments, while recombination in the core yields to a hydrodynamic expansion of lower-charge states [15].

We have conducted laser-based studies of short-wavelength pulsed interactions with clusters by converting light from a high-energy NIR femtosecond laser to the short-wavelength region through high-order harmonic generation [17]. In our experiments on Xe clusters irradiated by intense 38-nm XUV pulses, we observed results very similar to the DESY experiments: surprisingly high ion-charge states but with low kinetic energies. The directly measured kinetic-energy spectra showed that the clusters exploded by hydrodynamic forces rather than by Coulomb forces [17]. In this paper we extended the measurements to Ar clusters, including measurements of the energy distribution of the ejected electrons. They verified the nanoplasma model for rare-gas-cluster interactions in the XUV wavelength regime. Single-photon ionization and Lotz-type collisional ionization in conjunction with continuum lowered ionization potentials were identified as the dominating ionization processes.

II. EXPERIMENTAL PROCEDURE

We employed intense pulses of XUV light produced by high-harmonic generation (HHG) from an intense NIR femtosecond laser and refocused these pulses into a cluster-producing gas jet. The basic experimental layout of the higher harmonic beamline is presented in Ref. [17]. Figure 1 illustrates a closeup view of the cluster interaction chamber.

Because of the favorable scaling of harmonic yield with long focal length, the output of a 10-Hz chirped pulse amplified (CPA) Ti:sapphire system delivering 800-nm, 35-fs pulses of energy up to 100 mJ, was loosely focused into a pulsed jet of 200-psi argon with a 2-m focal length LiF lens ($f/60$) to an intensity of $\sim 10^{15}$ W/cm^2. Higher harmonic production was optimized by positioning the jet directly above the laser beam and 150 mm upstream of the focus. The pulsed gas jet consisted of a modified body of a Parker Series 9 valve with a

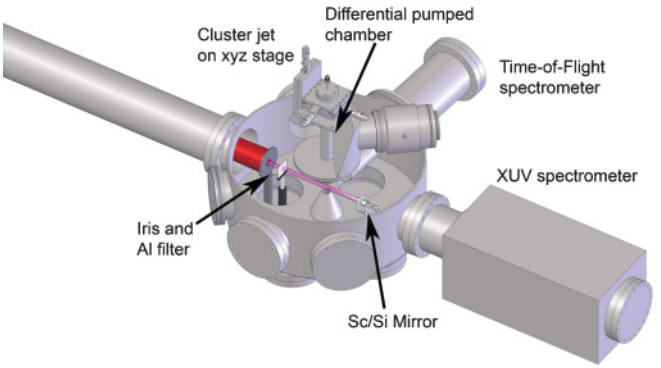

FIG. 1. (Color online) Illustration of the high-harmonic target chamber. XUV pulses of 38-nm light produced by harmonic conversion from the ir driving laser are isolated and refocused onto a rare-gas-cluster jet.

750-μm opening. An annular beam mask placed 4 m upstream of the lens obscured the central portion of the NIR pulse and was imaged to an iris 4 m after the lens to remove most of the infrared light. The mask was held by suspension wires; Fig. 2 shows the annular NIR profile in the image plane with an inner diameter of 12.5 mm and an outer diameter of 25 mm. After the beam diverges from the focus the annular ir light is blocked in the image plane by the iris. The near Gaussian, diffraction-limited HHG light is substantially less divergent than the driving beam, it expands "inside" the annulus and passes through the iris [18]. A 200-nm-thick Al filter (Luxel Corp.) blocked any residual NIR light from reaching the XUV interaction chamber. This technique avoided direct exposure and hence destruction of the filter with the intense driving NIR beam. After separating the NIR from the XUV harmonics, we selected and focused the 21st harmonic using a spherical Sc-Si multilayer mirror designed to reflect light at 38 nm $\pm$ 5 nm with $f/10$ geometry at near-normal incidence [19].

To measure the entire harmonic spectrum we replaced the multilayer mirror with a flat-field, grazing-incidence XUV spectrograph. The design is based on a mechanically ruled aberration-corrected concave grating [20] dispersing the

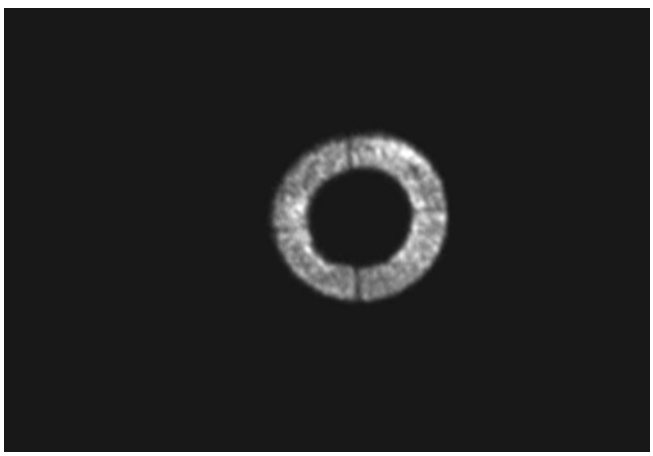

FIG. 2. Annular infrared profile in the image plane, with suspension wires visible. Inner diameter is 12.5 mm, outer diameter ~25 mm. Image is taken slightly off normal.

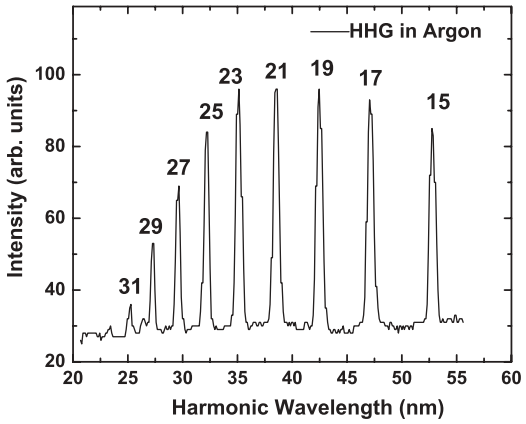

FIG. 3. Higher harmonics dispersed in a XUV spectrograph on a MCP-phosphor screen detector.

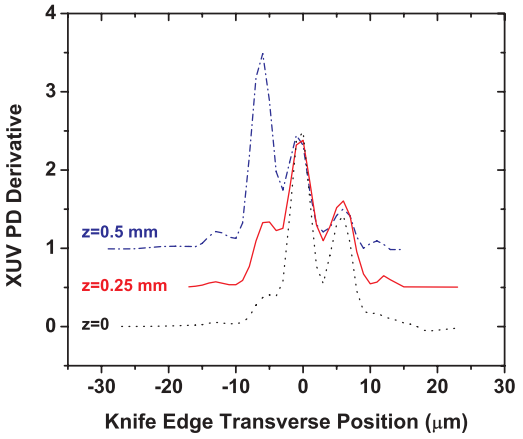

FIG. 5. (Color online) Derivatives of knife-edge measurement as a function of blade position through the focus.

higher harmonics onto a microchannel plate (MCP)-phosphor screen detector. Figure 3 shows a typical line out of the plateau and cutoff of harmonics produced in argon.

To measure the energy and spatial profile of the focused 21st harmonic, we positioned an XUV sensitive photodiode (IRD XUV-10) after the focus and scanned a knife edge perpendicular to the beam axis on different positions. The focused beam spot size of the 21st harmonic as a function of axial distance from the focusing mirror is shown in Fig. 4. The best-fit curve to a Gaussian spot size is also shown by the solid curve and implies an 8-μm beam diameter and a Rayleigh length of 120 μm. The data for the smallest focus sizes are illustrated in Fig. 5. The envelop fits to an 8-μm focal spot diameter ($1/e^2$ full width) as shown in our previous publication [17]. The substructure in the focus was discovered by decreasing the step size in the knife-edge scan, and it is caused by diffraction generated by the NIR annular beam shape. The total energy in the XUV beam after the focus was measured to be 0.5 nJ. Taking the substructure into account we determine that the peak XUV fluence is 7 mJ/cm^2. In Ref. [17] we assumed a 10-fs pulse duration for the HHG pulse from

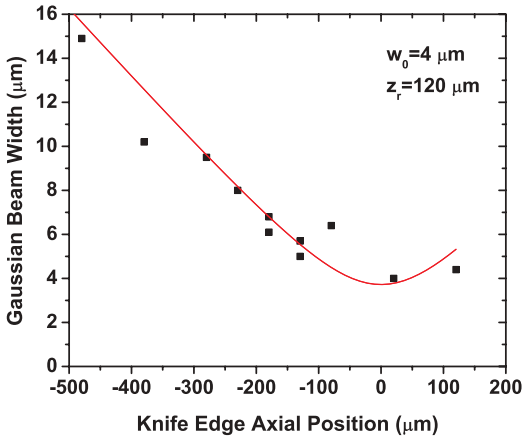

FIG. 4. (Color online) Focused beam spot size of the 21st harmonic as a function of axial distance from the focusing mirror. The best-fit curve to a Gaussian spot size is also shown by the solid curve.

our 35-fs full width at half maximum (FWHM) laser pulse, which implies a focal intensity of 7×10^{11} W/cm^2. As will be discussed below, we observed an aging effect in the multilayer mirrors leading to a less efficient suppression of neighboring harmonics. This addition of bandwidth in our experiment, with synchronizing of the adjacent harmonic components, enables the formation of a train of single-cycle subfemtosecond pulses as described by López-Martens *et al.* [21], leading potentially to intensities in the 10^{13} W/cm^2 range. However, the physics we believe that is important is linear, consequently peak intensity is less important than pulse fluence.

A second pulsed gas jet mounted directly above the XUV focus produced a jet of xenon or argon clusters. This jet used a modified conical 15° ($\Theta/2$) copper nozzle mounted on a Parker Series 9 solenoid pulsed nozzle, with a throat diameter of 500 μm, and was backed with a pressure of up to 25 bars. The nozzle was operated at a 10-Hz rate with an opening time of 1.2 ms. Using previously published results [22] to ascertain the cluster size created by pulsed supersonic jet expansion, we estimated that we produced a log-normal distribution [23] of clusters with an average size up to $\langle N\rangle \approx 10^5$ atoms. This was tunable by changing the gas backing pressure. The expanding gas includes a significant number of monomers, in recent measurements the degree of condensation for similar nozzles was determined to be ~20% [22,24].

In our early measurements of ion time-of-flight (TOF) spectra, we observed a significant broadening of the individual ion peaks. We attributed this to charge exchange between ions ejected by the clusters and surrounding neutral gas (the details of this effect are described in Ref. [26]). This broadening prevented direct analysis of ion kinetic energy from peak shapes. To reduce this broadening, a modified cluster beam source was implemented. Experiments were performed with the nozzle mounted above a 250-μm electroformed molecular-beam skimmer (Beam Dynamics, Inc.) in a differentially pumped expansion chamber. The skimmer produced a molecular beam ~1.5 mm in diameter at the XUV focus. This collimation limits the ionization region, reducing the collection of ions generated outside the XUV focus; however, the cluster beam is still larger than the XUV confocal parameter, so ions are collected in both high- and

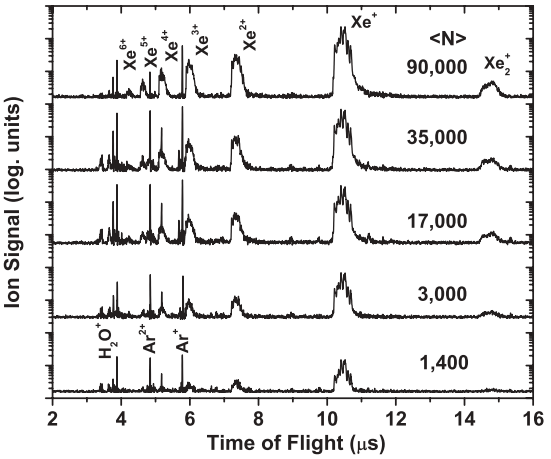

FIG. 6. Ion time-of-flight spectra of various exploding xenon cluster sizes at constant laser energy of 0.5 nJ.

low-intensity regions. The molecular-beam skimmer also greatly reduced the overall gas load on the target chamber, improving TOF resolution but at a cost of gas and cluster density in the focus because it is further from the nozzle aperture.

A Wiley-McLaren [25] TOF spectrometer was mounted relative to the XUV beam focus as shown in Fig. 1. A solid repeller plate prevented signal events from the unfocused XUV beam. Charged grids mounted around the XUV interaction region allowed us to measure the ion charge-state distribution. Extracted ions traveled through a field-free region to a dual MCP detector, whose output is recorded on an oscilloscope or a time-delay-counting card (P7886S, ComTec). When the extraction grids were grounded, the energetic ions from the explosions of the clusters traveled by their own initial kinetic energy to the MCP detector. In this way, a Xe ion energy spectrum could be recovered from the ion TOF. A mu-metal enclosure allowed us to measure electron spectra in the same configuration.

III. ION TIME-OF-FLIGHT MASS SPECTRA

Spectra of ions from the Xe clusters produced at various backing pressures (up to $N{\sim}10^5$) when irradiated with the 21st harmonic at constant intensity in the XUV focus are presented in Fig. 6. With the skimmer in place, we were able to resolve charge states up to Xe^{6+}, and we also observed the $Xe_2{}^+$ dimer. Purely atomic spectra are not shown because of their very small signal contribution at low gas densities, however, with the increasing expansion pressure (i.e., cluster size) the atomic density increases and shows a contribution in the cluster spectra in the form of narrow isotope peaks. Sequential single-photon ionization of atomic Xe is expected to generate Xe^{3+} but not higher-charge states. Charge states of 7 and 8 were not resolved and are overlapped by the water peak, but were shown in Ref. [17] in experiments without a skimmer. Note that there is a contribution of Ar^+ ions originating from gas flowing down from the HHG chamber to the XUV interaction region. As observed in earlier measurements [17] higher-charge states are produced when significant clusters begin to form in the jet. Although the abundance of highly charged ions is lower in our data than in the DESY results [6], we see the onset of highly charged ions (>3+) in the same cluster-size regime above the background gas.

Figure 7 shows a magnified spectrum for the biggest cluster size of $\langle N\rangle = 90\,000$. The isotope structure is clearly resolved examining the Xe^{1+} peak, demonstrating the suppression of secondary ions by the skimmer. Analyzing the peak shape, we see that every isotope shows a broadening mostly to shorter flight times because only forward and backward ejected ions from the interaction region will reach the detector [26]; ions ejected off axis are rejected by the TOF aperture. The shift in arrival times of the side peaks can be converted to kinetic energy by the TOF formula given by Wiley and McLaren [25], and is summarized in Fig. 7(b).

Argon clusters simplify the analysis of peak broadening, due to the dominance of the ^{40}Ar isotope (99.6%). The highest-charge state observed in significant quantity in our measurements is Ar^{4+}. The ^{36}Ar isotope is seen as an atomic peak as well in the dimer peak. Similar to the xenon spectra, the argon spectra show the same high-charge states with a lower abundance. An onset of broadening of the Ar peak at longer flight times occurs for larger clusters of argon. An example of this is observed in Fig. 8 for the Ar^+ peak at a flight time near 6.2 μs, and is due to an incomplete suppression of charge exchange with background gas by the skimmed setup as described above. This peak broadening was attributed to slow ions produced by a charge-transfer process

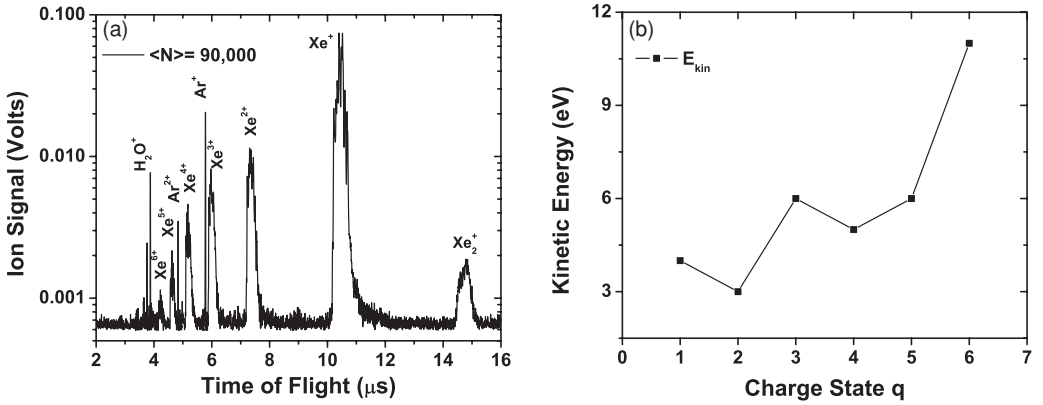

FIG. 7. (a) Expanded spectrum of exploding xenon cluster ions observed in a skimmed beam at a pulse energy of 0.5 nJ. (b) Broadening of xenon charge states converted to kinetic energy.

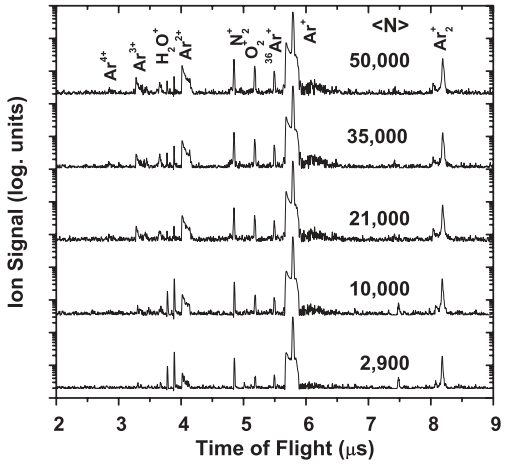

FIG. 8. Ion time-of-flight spectra of various exploding argon cluster sizes at constant laser energy of 0.5 nJ.

between extracted ions from the interaction region on their way to the detector with neutral surrounding jet atoms [26,27]. Figure 9 focuses on the forward and backward broadening of the Ar^{1+} peak shown as a function of the cluster size. The signal strength is increasing with the cluster size, but not the kinetic energy which corresponds to 3 eV. The kinetic energies for the higher-charge states are summarized in Fig. 10(b). The production of argon (as well as xenon) ions is biased in favor of the "forward" peak. Recombination from the charge-transfer process of backward-directed ions through the cluster jet causes suppression of the backward peak of ions Z^{n+}.

To ascertain whether collisional ionization alone can explain the data, we calculated the equilibrium charge-state distribution by numerical solution of the Saha equation for ions in a local thermal equilibrium (LTE) plasma. Figure 11(a) shows the calculated charge-state distribution for a solid-density xenon plasma at an 8-eV electron temperature [17]. We estimated a temperature of 8 eV for the electron gas in the nanoplasma from the resulting hydrodynamic explosion of the cluster; an analysis presented below. In a Xe plasma at this electron temperature there is an insignificant number of

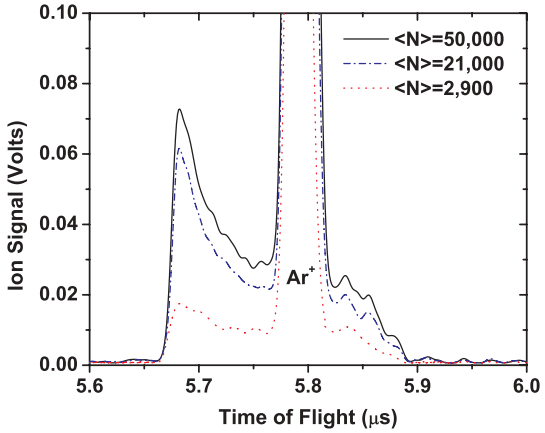

FIG. 9. (Color online) Broadening of the Ar^+ peak with increasing cluster size at constant laser energy.

ions with charge greater than 3+ that result from collisional ionization.

Earlier theoretical work [12] explained the high-charge states obtained in the DESY experiments as a result of the distortion of the ionic binding potential by neighboring charged ions. This picture is inaccurate in a quasineutral plasma, because the electrons will tend to shield the fields of the neighboring ions. A more recent paper includes the effects of the electron screening by including electrons removed by photoionization or electron collisions in high Rydberg orbits about the parent ion [30]. Though these numerical models by Georgescu *et al.* capture much of the physics determining the extent of the lowering of the ionization potential of ions in the cluster nanoplasma, it is possible to obtain quantitative insight from a straightforward analytic plasma model for the screening electrons. When an electron is removed from an ion in the plasma, it is not removed to infinity but is placed into the environment of the surrounding plasma. The repulsive energy of these electrons will reduce the effect of the attractive energy of the ion when removing subsequent electrons. In the most common model these continuum screening electrons are distributed in a Debye sheath about the parent ion. In our strongly coupled cluster nanoplasmas (where the strong coupling parameter $\Gamma \sim 0.7$), the usual Debye-Hückel model is not appropriate [31,32], but we can use the ion-sphere model [31] assuming that the electron distribution is uniform in a sphere of R_i in our cluster nanoplasma:

$$R_i = \left(\frac{3}{4\pi n_i}\right)^{1/3}. \tag{1}$$

If we assume the number of photoelectrons is retained in the ion sphere of each parent ion and their radial distribution about the ion is constant, we can calculate the change in Coulomb energy of the ion and its screening electrons during photoionization from ion state $z-1$ to z:

$$\Delta E_{\mathrm{CL}} = E^{z-1}_{\mathrm{Coul}} - E^{z}_{\mathrm{Coul}} = \frac{0.9(2z-1)e^2}{4\pi\varepsilon_0 R_i}. \tag{2}$$

We obtain values for continuum lowering shown in Table I assuming an ion-sphere radius of $R_i \sim n_i^{-1/3}$. The ionization potentials were taken from Refs. [33] and [34], and for n_i the liquid density was assumed. With this model we are able to explain the observed Xe charge states of up to 5+ seen in Fig. 7 and all of the observed Ar charge states in Fig. 10. Figure 11(b) shows the solution of the Saha equation for a Xe plasma when continuum lowering is included. The result reflects the corrected ionization potentials, but also shows the depletion of the lower-charge states. The fact that Eq. (2) overestimates the continuum lowering for the preferred R_i of Eq. (1) may result from assuming a strict charge neutrality within each ion sphere. At electron temperatures where a uniform radial distribution for screening is reasonable, the electron charge within each ion sphere may approach the mean charge per ion, $z' = \langle n_i z_i \rangle / \langle n_i \rangle$. Such a model replaces $(2z-1)$ with z' in Eq. (2) and gives values for continuum lowering close to those in Table I. The Debye screening length calculated from the 8 eV electron temperature determined later in this paper is much smaller than the ion sphere radius, requiring a detailed radial dependence for a more accurate model. Using numerical

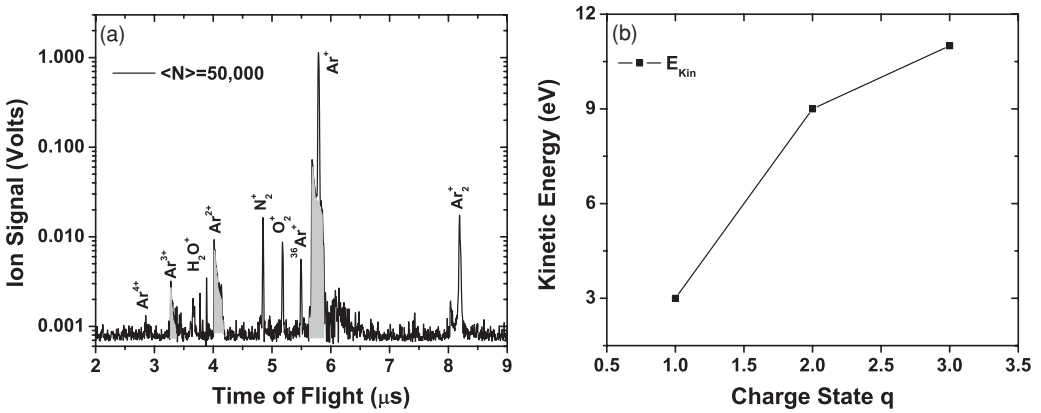

FIG. 10. (a) Expansion of the exploding argon cluster ion spectrum $\langle N \rangle = 50\,000$ for a laser-pulse energy of 0.5 nJ. (b) Broadening of the argon charge states converted to kinetic energy.

modeling, Ramunno [35] included both continuum lowering and the effect of excited states to predict ion-charge states that are in agreement with the experiment.

Taking the new ionization potentials into account the presence of a small number of xenon charge states with $z > 5+$ can then be explained by nonequilibrium collisional ionization of the Xe^{5+} ions produced rapidly (~20 fs) by the hot tail of the 8-eV electron distribution following photoionization during the XUV pulse. To calculate this rate we use the empirically determined collisional ionization rate formula of Lotz [36]. This rate per ion averaged over a Maxwellian electron distribution is

$$W_{kT} = n_e \frac{a_i q_i}{I_p} \sqrt{\frac{8}{\pi m_e k T_e}} \int_{I_p/kT_e}^{\infty} \frac{e^{-x}}{x} dx, \qquad (3)$$

where n_e is the electron density, I_p is the ionization potential in eV, a_i is an empirical constant equal to 4.0 $cm^2\ eV^2$, and q_i is the number of electrons in the outer shell of the ion. Using this formula with ionization potentials corrected by continuum lowering and an electron temperature of 8 eV, we calculate that roughly 5% of Xe^{5+} ions can be collisionally stripped up to Xe^{8+} during ~1.5 ps, the time for a 15-nm-diam, 8-eV cluster to expand hydrodynamically to roughly twice the initial radius. So the presence of small numbers of Xe^{6+}-Xe^{8+} in our data can be explained by electron collisional ionization from the photoionized Xe^{5+} state.

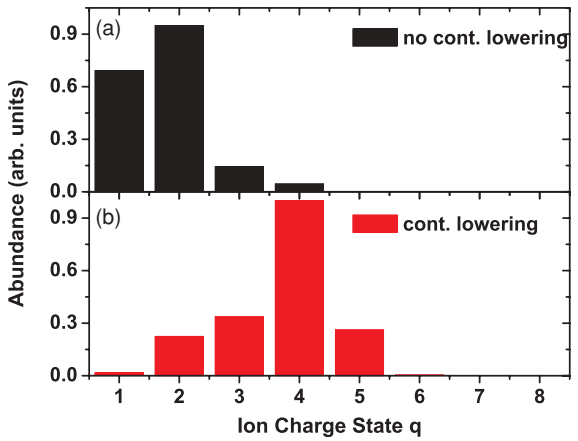

FIG. 11. (Color online) The equilibrium charge-state distribution from a Xe plasma at $T_e = 8$ eV found by numerical solution of the Saha equation (a) based on Xe ionization potentials and (b) continuum lowering included.

IV. ION KINETIC-ENERGY MEASUREMENTS

The next question that we wished to address was whether these highly charged ions in the cluster exploded by a Coulomb explosion, as has been surmised by the DESY group in their results with VUV pulses [6,7]. To do this we examined the energy spectrum from the exploding Xe clusters by field-free TOF analyses of the ejected ions as described in the Introduction. It was not possible to collect a spectrum with a skimmer after the nozzle because of the very small signal. For this measurement the jet nozzle was placed 1 cm above the grounded extraction grids. Figure 12 shows the energy spectrum of Xe ions ejected from the exploding clusters when the average cluster size is 30 000 atoms. This ion distribution peaks at ~80 eV and has a tail that extends out toward 400 eV. The large number of ions <20 eV is responsible for the peak broadening in the mass over charge-resolved spectra, which were extracted in Fig. 7(b). The decrease in the number of ions in the distribution near the atomic ionization potential may result from collisions with the background gas produced by removal of the skimmer.

If the explosion of clusters is driven by Coulomb forces, the ion-energy spectrum from a single exploding cluster can

TABLE I. Ionization potentials and calculated amounts of continuum lowering for Xe and Ar nanoplasmas in eV units.

z	1	2	3	4	5	6	7	8
I_p Xe	12.13	21.97	31.05	40.9	54.14	66.7	91.6	105.98
ΔE_{CL}	3	9	15	21	27	33		
I_p Ar	15.76	27.63	40.74	59.81	75.02			
ΔE_{CL}	4.5	9	13.5	31.5	40.5			

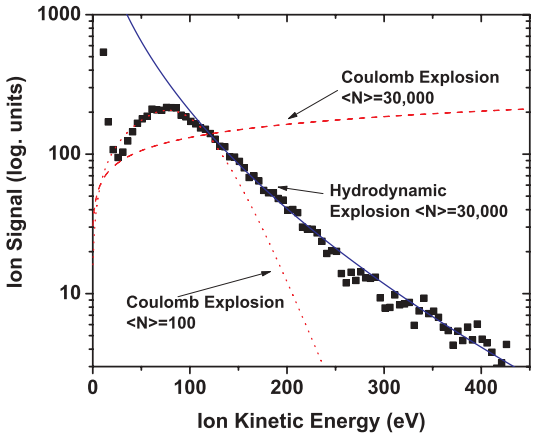

FIG. 12. (Color online) Measured Xe ion kinetic-energy spectrum of exploding $\langle N\rangle \sim 30\,000$ clusters. Fitted lines correspond to models of Coulomb explosion for small (dotted line) and big clusters (dashed line) and hydrodynamic cluster explosion with $T_e = 8$ eV for $\bar{z} = 1.75$ (solid line).

be written as [4]

$$f(E)\,dE \propto \begin{cases} E_{\max}\sqrt{E} & \text{for} \quad E \leqslant E_{\max}, \\ 0 & \text{for} \quad E > E_{\max}, \end{cases} \tag{4}$$

$$E_{\max} = \frac{z^2 e^2}{3\varepsilon_0} n_i R_0^2, \tag{5}$$

where $E_{\max}$ is the maximum energy for ejected ions from the cluster surface. We can calculate the spectrum from Coulomb exploding clusters by convolving the spectrum of a single Coulomb exploding cluster with a log-normal cluster-size distribution, a procedure which has been shown to model accurately the explosions of deuterium clusters irradiated by high-intensity 800-nm laser pulses [4]. The calculated spectrum for Coulomb exploding clusters with $\langle N\rangle = 30\,000$ (and $\bar{z} = 1.75$) is illustrated in Fig. 12. This distribution is very different than the observed spectrum with a peak well above 2 keV. For comparison, the spectrum from a best-fit distribution with $\langle N\rangle = 100$ is also illustrated in this figure. Such a Coulomb explosion distribution matches the shape of the ion spectrum peak at 80 eV but does not accurately match the tail of the energy distribution. On the other hand, we have fitted our observed ion spectrum to that of a hydrodynamically expanding quasineutral cluster nanoplasma using the well-known self-similar solution of ion energies resulting from an isothermal expansion [28]:

$$f(E)\,dE \propto \exp -\sqrt{E/zk_B T_e}. \tag{6}$$

The best fit passes through the data over the entire energy range from 100 to 400 eV and is consistent with an initial electron temperature in the Xe cluster plasma of 8 eV for an average charge state of $\bar{z} = 1.75$ determined from the ion mass over charge spectrum shown in Fig. 7(a). This electron temperature is very close to that of the electron spectrum observed in Ref. [8] from VUV FEL irradiation of Xe and Ar clusters. The observed ion-energy spectrum is strong evidence that a near quasineutral nanoplasma is formed under XUV pulse irradiation of the Xe cluster and that the explosion mechanism is not by Coulomb explosion but instead by hydrodynamic expansion.

We calculated the energy input in our xenon cluster by IBS in the XUV field by using the IBS absorption rate κ_α derived by Zel'dovich and Raizer for high-energy photons [29]:

$$k_\alpha[\mathrm{cm}^{-1}] = 3.69 \times 10^8 \frac{z^2}{\sqrt{T[\mathrm{K}]}\nu^3} n_i n_e. \tag{7}$$

The amount of energy per electron is given by

$$E[\mathrm{eV}] = (k_\alpha \phi \Delta t h\nu)/n_e, \tag{8}$$

where ϕ is the photon flux in $\mathrm{cm}^{-2}\mathrm{s}^{-1}$, Δt is the XUV pulse length, and $h\nu$ is the photon energy in eV. For an initial electron temperature of 0.1 eV we calculated an energy rise for the distribution of only 0.05 eV during the laser pulse. An observed temperature of 8 eV is completely inconsistent with the amount of heating we expect by IBS in the XUV field. Photoionization heating is much more likely, a process which refers to the energy given to electrons through each photoionization event. Each photoionization to Xe^+, for example, generates an electron with 20.5 eV. When averaging over all ion states shown in Fig. 7, and the corrected ionization potentials from Table I, we calculated a much closer mean energy for the ejected electrons of 19.7 eV.

V. ELECTRON KINETIC ENERGY MEASUREMENTS

Electron kinetic energy spectra of exploding xenon and argon clusters were also measured with the TOF apparatus and are shown in Figs. 13 and 14. Photoelectron peaks with an energy characterized by direct single-photon ionization of background and cluster atoms by the 21st harmonic were clearly observed. We also observed "sidebands" on these photoelectron peaks revealing the presence of adjacent harmonics in the XUV focus. This passage of adjacent harmonics was attributed to the degradation in reflectivity of the aging Sc-Si mirror. More significantly, a large, low-energy background below 10 eV is seen in the electron spectra, which we interpret as a contribution from the expanding nanoplasma. No electrons

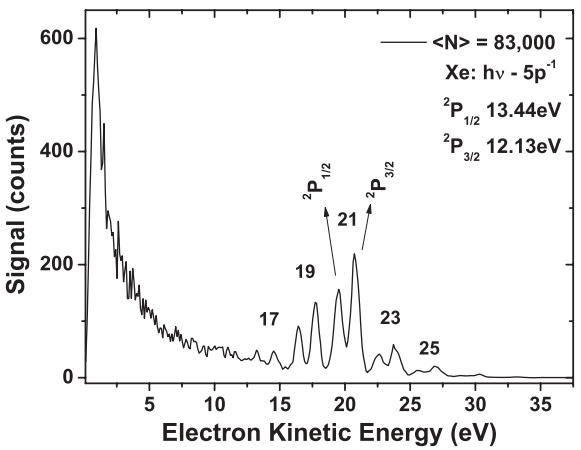

FIG. 13. Exploding xenon cluster $\langle N\rangle = 83\,000$ electron kinetic energy spectrum following 0.5-nJ XUV excitation at 32.6 eV. The double peak structure is due to $^3P_{1/2}$-$^3P_{3/2}$ spin-orbit splitting in the xenon ion.

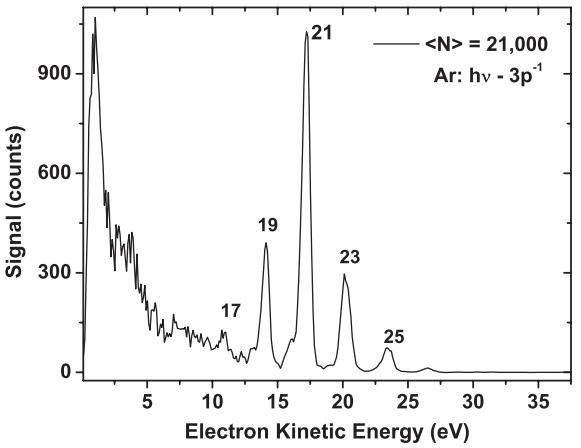

FIG. 14. Exploding argon cluster $\langle N\rangle = 21\,000$ electron kinetic-energy spectrum following 0.5-nJ XUV excitation at 32.6 eV.

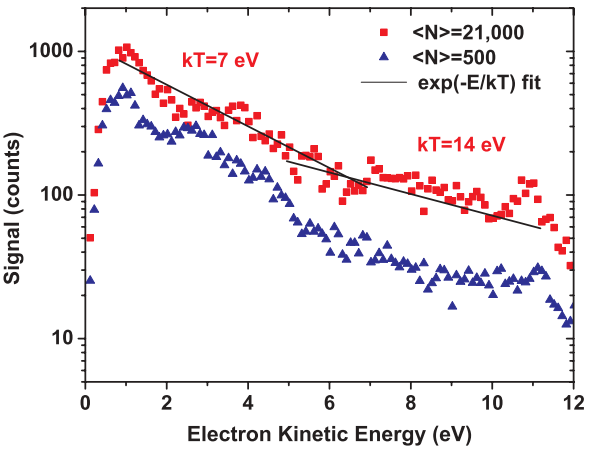

FIG. 16. (Color online) Low kinetic-energy distribution for small, $\langle N\rangle = 500$, and big, $\langle N\rangle = 21\,000$, exploding argon clusters. Solid lines represent best fits for electron temperatures.

with energy significantly higher than the excess photoelectron energy ($h\nu - I_p$) are observed.

In xenon, the peak resulting from each harmonic is split into two peaks due to the spin-orbit splitting ($^3P_{1/2}$-$^3P_{3/2}$) of the ion, as illustrated in Fig. 13. The line splitting of 1.3 eV determines the resolution of the spectrometer in this energy range. The line splitting for argon is smaller (∼0.4 eV) and cannot be resolved, as shown in Fig. 14. With this resolution, we were unable to detect cluster-influenced energy shifts from valence-band structures that are commonly observed in experiments on synchrotron sources (e.g., Ref. [37] and references therein). The low-energy electron feature at <10 eV is nonetheless also observed in the Ar data. Figures 15 and 16 show an expanded view of the low-energy contribution of the electron spectra. They are fitted to a Boltzmann intensity distribution. An electron-energy contribution of 7 eV is in excellent agreement to the temperature obtained by the hydrodynamic model from the ion kinetic energy data.

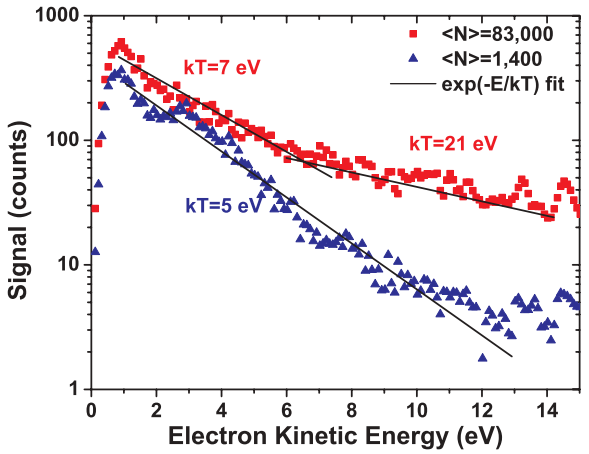

FIG. 15. (Color online) Low kinetic-energy distribution for small, $\langle N\rangle = 1400$, and big, $\langle N\rangle = 83\,000$, exploding xenon clusters. Solid lines represent best fits for electron temperatures.

VI. DISCUSSION AND CONCLUSION

In summary, we used the process of high-order harmonic-frequency conversion to study cluster explosions in the XUV wavelength range. To optimize the high-harmonic production in an argon jet we applied loose focusing, an annular beam technique, and multilayer optics. By exposing large clusters of noble gases of xenon and argon to the generated intense XUV pulses, we have produced ions with charge states and kinetic energy far above the single-photon limit. These interactions result from the collective response of nanoscale clusters to the intense applied field. Continuum lowering in the generated nanoplasma enables high-charge states to be reached by single photoionization. The small number of charge states above the single photoionization limit can be explained by additional nonequilibrium collisional electron ionization. Ion and electron kinetic-energy spectra revealed that a hydrodynamic model is appropriate for the explosion of clusters exposed to intense XUV short-wavelength radiation. We showed that IBS is not expected to be a significant heating mechanism in this wavelength range, but that photoionization heating can be responsible for the observed plasma temperature. These findings extend and complement earlier measurements, performed from the VUV to the soft x-ray range at the DESY FEL, which concluded that shorter wavelengths will decrease the influence of laser heating. Our data is especially important for the mid XUV range where the only data available from the FEL so far was for small, <200 atoms, argon clusters [9]. The common picture of both experiments is the nanoplasma generation and a minor importance of IBS heating, while differences can be attributed to larger cluster sizes used in our experiment.

ACKNOWLEDGMENT

This work was supported by the DOE Office of Basic Energy Sciences and the National Nuclear Security Administration under Cooperative agreement No. DE-FC52-03NA00156.

[1] T. Ditmire, T. Donnelly, A. M. Rubenchik, R. W. Falcone, and M. D. Perry, Phys. Rev. A **53**, 3379 (1996).
[2] M. Lezius, S. Dobosz, D. Normand, and M. Schmidt, Phys. Rev. Lett. **80**, 261 (1998).
[3] T. Ditmire *et al.*, Nature (London) **386**, 54 (1997).
[4] K. W. Madison *et al.*, Phys. Plasmas **11**, 270 (2004).
[5] R. Neutze *et al.*, Nature (London) **406**, 752 (2000).
[6] H. Wabnitz *et al.*, Nature (London) **420**, 482 (2002).
[7] T. Laarmann, A. R. B. de Castro, P. Gürtler, W. Laasch, J. Schulz, H. Wabnitz, and T. Möller, Phys. Rev. Lett. **92**, 143401 (2004).
[8] T. Laarmann, M. Rusek, H. Wabnitz, J. Schulz, A. R. B. de Castro, P. Gurtler, W. Laasch, and T. Möller, Phys. Rev. Lett. **95**, 063402 (2005).
[9] C. Bostedt, H. Thomas, M. Hoener, and E. Eremina, Phys. Rev. Lett. **100**, 133401 (2008).
[10] H. Thomas *et al.*, J. Phys. B **42**, 134018 (2009).
[11] R. Santra and C. H. Greene, Phys. Rev. Lett. **91**, 233401 (2003).
[12] C. Siedschlag and J. M. Rost, Phys. Rev. Lett. **93**, 043402 (2004).
[13] D. Bauer, J. Phys. B: At. Mol. Opt. Phys. **37**, 3085 (2004).
[14] C. Jungreuthmayer *et al.*, J. Phys. B **38**, 3029 (2005).
[15] B. Ziaja, H. Wabnitz, F. Wang, E. Weckert, and T. Möller, Phys. Rev. Lett. **102**, 205002 (2009).
[16] B. N. Breizman, A. V. Arefiev, and M. V. Fomyts'kyi, Phys. Plasmas **12**, 056706 (2005).
[17] B. F. Murphy, K. Hoffmann, A. Belolipetski, J. Keto, and T. Ditmire, Phys. Rev. Lett. **101**, 203401 (2008).
[18] J. Peatross *et al.*, Opt. Lett. **19**, 942 (1994).
[19] Y. A. Uspenskii *et al.*, Opt. Lett. **23**, 771 (1998).
[20] T. Kita *et al.*, Appl. Opt. **22**, 512 (1983).
[21] R. López-Martens *et al.*, Phys. Rev. Lett. **94**, 033001 (2005).
[22] F. Dorchies, F. Blasco, T. Caillaud, J. Stevefelt, C. Stenz, A. S. Boldarev, and V. A. Gasilov, Phys. Rev. A **68**, 023201 (2003).
[23] M. Lewerenz, B. Schilling, and J. P. Toennies, Chem. Phys. Lett. **206**, 381 (1993).
[24] A. V. Arefiev *et al.*, High Energy Density Phys. **6**, 121 (2010).
[25] W. C. Wiley and I. H. McLaren, Rev. Sci. Instrum. **26**, 1150 (1955).
[26] K. Hoffmann *et al.*, High Energy Density Phys. **6**, 185 (2010).
[27] J. B. Hasted and M. Hussain, Proc. Phys. Soc. London **83**, 911 (1964).
[28] R. F. Schmalz, Phys. Fluids **28**, 2923 (1985).
[29] Ya. B. Zel'dovich and Yu. P. Raizer, *Physics of Shock Waves and High Temperature Hydrodynamic Phenomena* (Dover, Mineola, NY, 2002), p. 259.
[30] I. Georgescu, U. Saalmann, and J. M. Rost, Phys. Rev. A **76**, 043203 (2007).
[31] R. P. Drake, *High Energy Density Physics: Fundamentals, Inertial Fusion and Experimental Astrophysics* (Springer Verlag, Berlin, 2006), p. 73.
[32] G. Ecker and W. Kroell, Phys. Fluids **6**, 62 (1963).
[33] E. B. Saloman, J. Phys. Chem. Ref. Data **33**, 3 (2004).
[34] C. E. Moore, NSRDS, Natl. Bur. Stand. **34**, 22 (1970).
[35] L. Ramunno *et al.* (private communication).
[36] W. Lotz, Z. Phys. **206**, 205 (1967).
[37] D. Rolles *et al.*, Chem. Phys. Lett. **468**, 148 (2009).